nature communications

Article

https://doi.org/10.1038/s41467-024-54311-0

Improved conduction and orbital polarization in ultrathin $LaNiO_3$ sublayer by modulating octahedron rotation in $LaNiO_3$/$CaTiO_3$ superlattices

Received: 27 February 2024

Accepted: 4 November 2024

Published online: 15 November 2024

Check for updates

Wenxiao Shi[1,2,7], Jing Zhang[3,7], Bowen Yu[1,2,7], Jie Zheng[1,2], Mengqin Wang[1,2], Zhe Li[1,2], Jingying Zheng[4], Banggui Liu[1,2] ✉, Yunzhong Chen[1,2], Fengxia Hu[1,2], Baogen Shen[1,2,5], Yuansha Chen[1,2] ✉ & Jirong Sun[1,2,6] ✉

Artificial oxide heterostructures have provided promising platforms for the exploration of emergent quantum phases with extraordinary properties. Here, we demonstrate an approach to stabilize a distinct oxygen octahedron rotation (OOR) characterized by $a^-a^-c^+$ in the ultrathin $LaNiO_3$ sublayers of the $LaNiO_3$/$CaTiO_3$ superlattices. Unlike the $a^-a^-c^-$ OOR in the $LaNiO_3$ bare film, the $a^-a^-c^+$ OOR favors high conductivity, driving the $LaNiO_3$ sublayer to a metallic state of ~100 K even when the layer thickness is as thin as 2 unit cells (u.c.). Simultaneously, strongly preferred occupation of $d_{x^2-y^2}$ orbital is achieved in $LaNiO_3$ sublayers. The largest change of occupancy is as high as 35%, observed in the 2 u.c.-thick $LaNiO_3$ sublayers sandwiched between 4 u.c.-thick $CaTiO_3$ sublayers. X-ray absorption spectra indicate that the $a^-a^-c^+$ OOR pattern of $LaNiO_3$ achieved in the $LaNiO_3$/$CaTiO_3$ heterostructures has significantly enhanced the Ni-3d/O-2p hybridization, stabilizing the metallic phase in ultrathin $LaNiO_3$ sublayers. The present work demonstrates that modulating the mode of OOR through heteroepitaxial synthesis can modify the orbital-lattice correlations in correlated perovskite oxides, revealing hidden properties of the materials.

Perovskite-structured rare-earth nickelates ($ReNiO_3$) have attracted great research interest due to their electronic transport and magnetic properties arising from the strong correlation of the Ni 3d orbitals[1,2]. Among the $ReNiO_3$ family, $LaNiO_3$ (LNO) is particularly interesting since it is the only member that maintains paramagnetic and metallic at all temperatures while other rare-earth nickelates undergo a metal-insulator transition (MIT) as temperature decreases[3,4]. Previous studies proved that the different transport properties largely originated from the different degrees or patterns of the NiO_6 oxygen octahedron rotation (OOR)[5–7]. LNO possesses a rhombohedral structure with the space group $R\bar{3}C$, in which the NiO_6 octahedra tilt and rotate in the manner of $a^-a^-a^-$ in the Glazer notation[8–10]. In contrast, other $ReNiO_3$ compounds usually have an orthorhombic structure (space group Pbnm) with the $a^-a^-c^+$-typed OOR[5–7,11]. The different OOR patterns will result in different Ni-O-Ni bond angles in the nickelates, affecting the hybridization between

[1]Beijing National Laboratory for Condensed Matter Physics and Institute of Physics, Chinese Academy of Sciences, Beijing, China. [2]School of Physical Sciences, University of Chinese Academy of Sciences, Beijing, China. [3]Songshan Lake Materials Laboratory, Dongguan, Guangdong, China. [4]College of Materials Science & Engineering, Fuzhou University, Fuzhou, China. [5]Ningbo Institute of Materials Technology & Engineering, Chinese Academy of Sciences, Ningbo, Zhejiang, China. [6]School of Materials Science & Engineering, Taiyuan University of Science and Technology, Taiyuan, China. [7]These authors contributed equally: Wenxiao Shi, Jing Zhang, Bowen Yu. ✉e-mail: bgliu@iphy.ac.cn; yschen@iphy.ac.cn; jrsun@iphy.ac.cn

Ni-3d and O-2p orbitals thus the transport behavior of the nickelates[12–14].

An active topic on LNO is the control of orbital polarization. As well established, the basic band structure of the high *Tc* superconducting cuprates is that of a two-dimensionality (2D) single-band of Cu $d_{x^2-y^2}$ with spin one half and strong antiferromagnetic correlations[15–17]. Ni^{3+} ions in LNO possess a $3d^7$ electron configuration, with a fully occupied t_{2g} shell and one electron occupied the e_g state. However, the e_g orbitals of bulk LNO are doubly degenerated[18–20]. Previous theoretical studies have predicted that the ultrathin LNO layer sandwiched between two insulating layers could present the analogous electronic structure to cuprates, i.e. an ordering of the planar $d_{x^2-y^2}$ orbitals that confine electronic transport to two dimensions[21,22]. Due to this similarity, LNO-based oxide heterostructures are believed to be candidates of high-temperature superconductors. However, this expectation has not been fulfilled till now for the following reasons. Firstly, the measured orbital polarization in LNO-based heterostructures is much smaller than that of theoretical prediction[18,23–26]. Possibly, the strong hybridization between Ni-3d and O-2p bands has resulted in a $3d^8\underline{L}$ state in LNO ($\underline{L}$ denotes a ligand hole on the oxygen ion), which is not susceptible to orbital polarization. Secondly, the LNO layer, either in the form of a bare film or a sublayer of superlattice (SL), becomes insulating when it is reduced to a few unit cells (u.c.) in thickness. For example, the critical thickness for the metallic LNO layer is ~3 u.c. under the compressive strain imposed by LAO substrate or ~5 u.c. under the tensile strain of $SrTiO_3$ (STO) substrate[19,27–30]. Anderson localization induced by strain effect and reduced dimensionality is believed to be the mechanism for the strongly insulating behavior in ultrathin LNO layers[31,32]. Obviously, the simultaneous achievement of a metallic behavior and a larger orbital polarization in ultrathin LNO layers is the prerequisite for the realization of LNO-based superconductivity.

Perovskite titanates $CaTiO_3$ (CTO) is an insulating oxide that has very similar pseudocubic lattice parameter with LNO (3.81 Å vs 3.83 Å). The TiO_6 octahedra in the CTO films are usually orthorhombically distorted, with the $a^-b^+a^-$-typed OOR[33,34]. As mentioned above, the OOR has played an important role in determining the transport behavior of nickelates. As schematically shown in Fig. 1a, when grouping LNO ($a^-a^-a^-$) and CTO ($a^-b^+a^-$) layers together to form a heterostructure, the strong OOR mismatch between LNO and CTO, i.e., the in-phase (b^+) or out-of-phase (a^-) rotation along the **b** axis, may produce distinct proximity effect, modulating the transport behavior of the ultrathin LNO.

In this work, we demonstrate an approach to stabilize a nonequilibrium OOR in the form of $a^-a^-c^+$ in the LNO sublayers of the LNO/CTO SLs. In sharp contrast to the $a^-a^-c^-$ pattern, the $a^-a^-c^+$ OOR is found to favor the metallic state of the LNO layer with a thickness down to 2 u.c.. More than that, a strong $d_{x^2-y^2}$ orbital polarization is achieved in the LNO sublayers. The largest change of occupancy is as high as 35%, observed in the SL with 2 u.c.-thick LNO and 4 u.c.-thick CTO sublayers. X-ray absorption spectra indicate that the modulated OOR pattern of LNO in the LNO/CTO SLs has significantly enhanced the Ni-3d/O-2p hybridization, stabilizing the metallic state in LNO ultrathin films. Our work suggests that engineering the nonequilibrium OOR pattern by heteroepitaxial synthesis is a feasible avenue to modify the orbital-lattice correlation in correlated systems, unveiling hidden aspects of oxide materials.

Results

Structural analysis of LNO/CTO superlattice

$[LNO_m/CTO_n]_8$ (L_m/C_n) SLs formed by alternately stacking LNO and CTO layers were epitaxially grown on (001)-oriented STO or LSAT substrates by the technique of pulsed laser deposition. Each period of the SL is composed of *m* unit cells of LNO and *n* unit cells of CTO, where *m* ranges from 2, 3 to 4, and *n* takes 1, 2, or 4. The out-of-plane lattice structure of the SLs was analyzed by x-ray diffraction (XRD) spectra as shown in Fig. 1b and Supplementary Fig. 1. The clear (001) Bragg peaks with thickness fringes indicates the good crystallinity and flat surface of the samples, which is also confirmed by the atomic force microscopy image in Supplementary Fig. 1a. Moreover, distinct satellite peaks are detected, in agreement with the designed structure period. The satellite peaks shift towards the (001) main peak as *m* and *n*

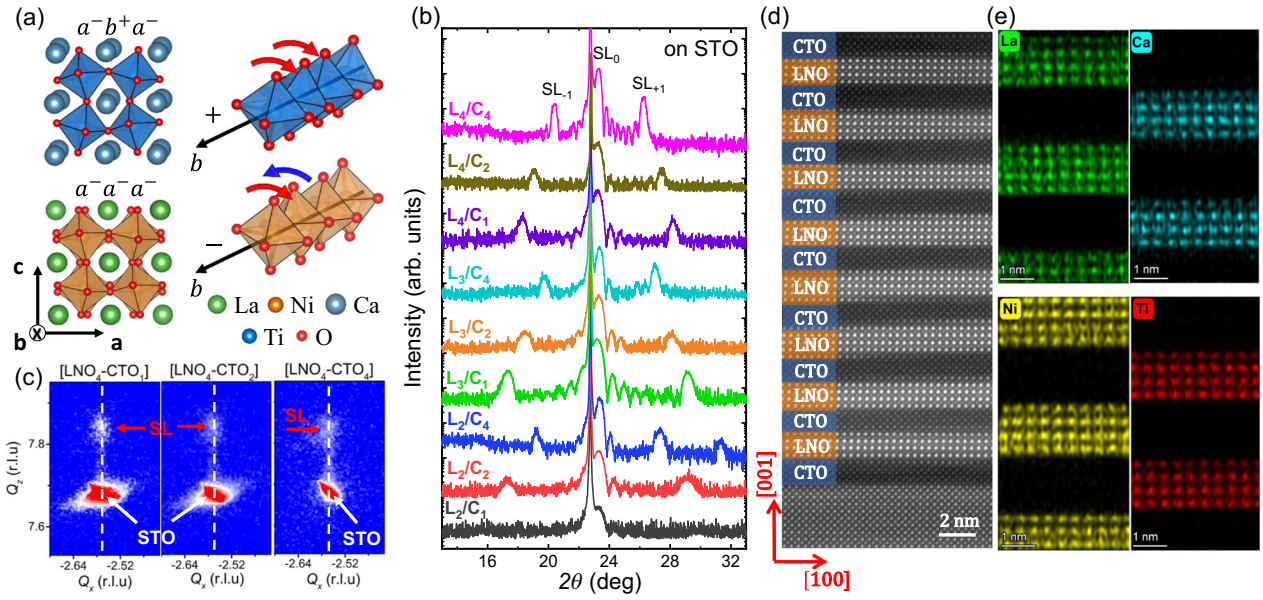

Fig. 1 | Structural characterizations of LNO/CTO SLs. a Schematic views of lattice structures of CTO with an $a^-b^+a^-$ OOR pattern (up panel) and LNO with an $a^-a^-a^-$ OOR pattern (bottom panel). Blue and orange octahedra represent TiO_6 and NiO_6, respectively. The right panel shows the in-phase rotation (b^+) and out-of-phase rotation (a^-) along the **b**-axis for the CTO and LNO, respectively. **b** Out-of-plane θ–2θ scans for the L_m/C_n SLs on (001)-oriented STO substrate. SL_0 indicates the (001) main peak and SL_{-1}, SL_{+1} indicate the satellite peaks. **c** RSM spectra around (103) reflection measured for the L_4/C_1, L_4/C_2 and L_4/C_4 SLs. **d** High-angle annular dark-field (HAADF) image of the cross-section of the L_4/C_4 SLs, recorded along [100] zone axis. The LNO and CTO sublayers are marked by orange and blue colors, respectively. **e** The elemental EDS maps extracted from spectral images with a selected EDS energy window for each element: La, Ca, Ni, Ti.

https://doi.org/10.1038/s41467-024-54311-0

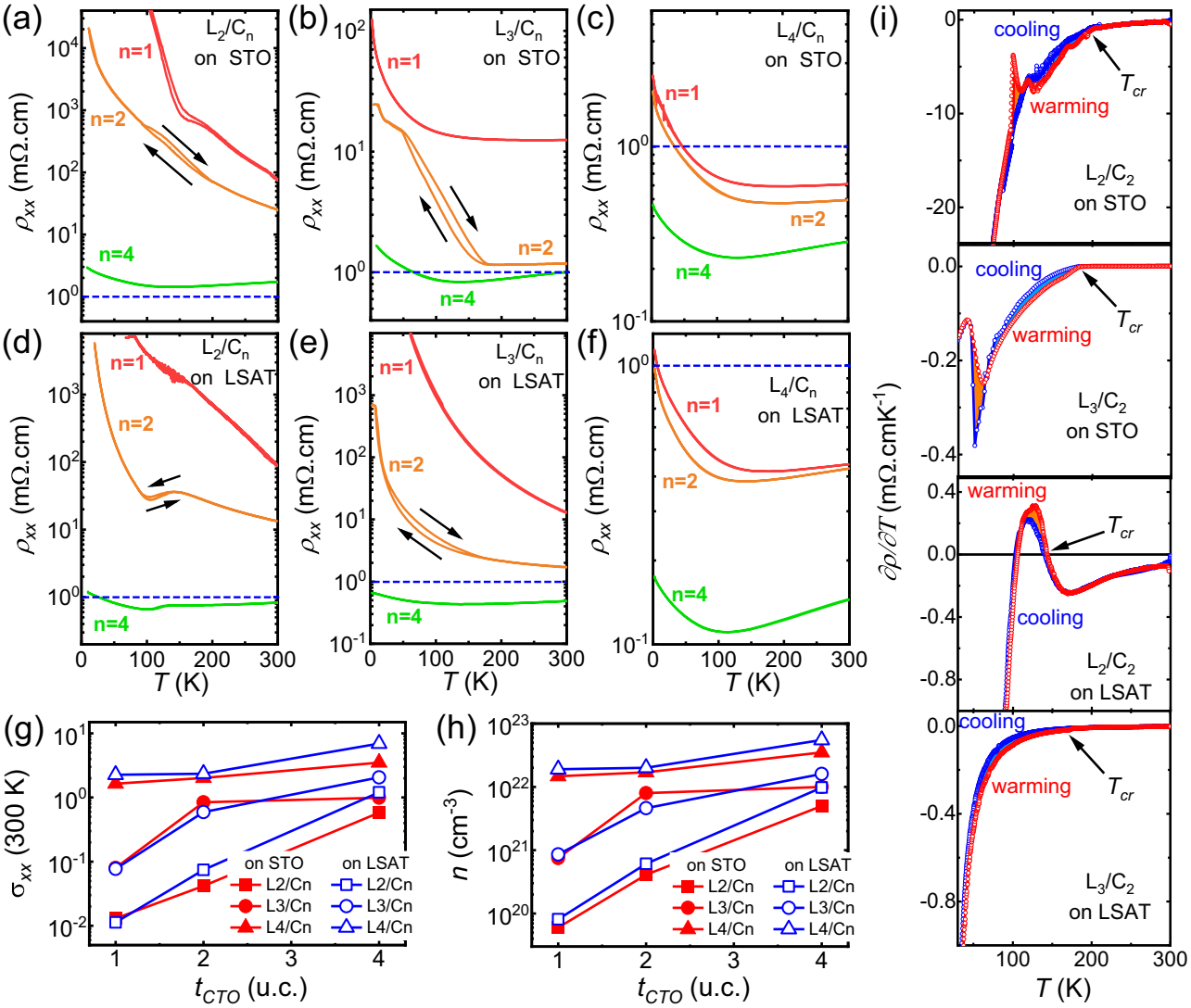

Fig. 2 | Transport behaviors of LNO/CTO SLs. a ρ_{xx}-T curves for the L_2/C_n, **b** L_3/C_n, and **c** L_4/C_n SLs on STO substrate. **d** ρ_{xx}-T curves for the L_2/C_n, **e** L_3/C_n and **f** L_4/C_n SLs on LSAT substrate. n represents 1, 2, and 4. The blue dashed lines represent $\rho_{xx} = 1\ m\Omega{\cdot}cm$. **g** Conductivity ($\sigma_{300}$) and **h** carrier density (n) of the L_m/C_n SLs as functions of t_{LNO} (m u.c.) and t_{CTO} (n u.c.), measured at 300 K. The data with red or blue color indicates the results of SLs on STO or LSAT, respectively. **i** The first derivative of resistivity with respect to temperature ($d\rho/dT$) for typical SL samples. The T_{cr} label indicates where the hysteresis begins to appear in the cooling process.

increases, which is a general feature of the XRD spectra for SL structures. To further determine the in-plane strain state of the SLs, the reciprocal space mapping (RSM) of the (103) reflection is measured. Taking L_4/C_n series SLs as an example, the diffraction spots of the SL (marked by the red arrow in Fig. 1c) are located just above that of the STO, i.e., all the SLs are coherently strained to the substrate without lattice relaxation. This conclusion is also applicable to other samples.

To get information on atomic arrangements, the lattice structure of the SL is further investigated by the high-resolution scanning transmission electron microscope (STEM). Figure 1(d) presents the high-angle annular dark-field (HAADF) lattice image of the cross-section of the L_4/C_4 SL, recorded along the [100] zone axis. Due to the strong brightness contrast between La and Ca atoms, the alternate stacking of LNO and CTO layers along the [001] direction is clearly seen, confirming the coherent and epitaxial growth of the periodic structure with atomically flat interfaces (detailed line profile analysis see Supplementary Fig. 2). Figure 1e provides layer-resolved energy-dispersive x-ray spectroscopy (EDS) mappings from a local area (approximately two SL periods) of the HAADF image. The sub-lattices of the A-site (La, Ca) and B-site (Ni, Ti) ions show sharp interfaces between LNO and CTO layers, without signatures of cation intermixing and layer dislocations. All these results indicate the high quality of SLs with well-ordered target structures.

Metallic behavior achieved in ultrathin LNO layer

To evaluate the influence of interface coupling, the transport properties of SLs are investigated. Figure 2a–c shows the longitudinal resistivity as a function of temperature (ρ_{xx}-T) for the L_m/C_n SLs on STO, where m and n range from 2 to 4 and from 1 to 4, respectively. The L_2/C_1 SL with the thinnest LNO and CTO sublayers shows a strongly localized behavior, exhibiting a resistivity that quickly increases upon cooling. When fixing the layer thickness of LNO to 2 u.c. whereas increasing the layer thickness of CTO, a significant decrease in resistivity appears. For example, the resistivity at 300 K (ρ_{300}) is 76.6 $m\Omega{\cdot}cm$ for the L_2/C_1 SL, 23.9 $m\Omega{\cdot}cm$ for the L_2/C_2 SL, and 1.7 $m\Omega{\cdot}cm$ for the L_2/C_4 SL. More importantly, the metallic behavior is clearly identified for the L_2/C_4 SL in the temperature range from 300 K to 130 K, though a slight resistive upturn appears at low temperatures. Similar phenomena are also observed in the L_3/C_n and L_4/C_n series of SLs. These results are unexpected, being in stark contrast to the insulating behavior of the 4 u.c.-thick LNO bare films (see Supplementary Fig. 3). They suggest an increase, rather than decrease, in the conductivity of LNO as the

thickness of the CTO layer increases, i.e., the LNO layers become more conductive when they are separated by thicker CTO layers.

The x-ray absorption spectra (XAS) around the Ni L_3 edge and Ti $L_{2,3}$ edge of the SLs are given in Supplementary Fig. 4. The good vertical alignment of the Ni L_3 edge and Ti $L_{2,3}$ edge peaks suggests that there is no charge transfer at the LNO/CTO interface, being consistent with the results reported for the $NdNiO_3/SrTiO_3$ SL[35]. It means that the CTO layers remain highly insulating in the SLs since Ti ions maintain a +4-oxidation state[18,36], regardless of the thickness of either the LNO or CTO sublayer. Thus, it is unusual that the resistivity of the L_m/C_n SLs is lowered by increasing the layer thickness of the CTO. To further check the strain effect on such an anomaly, the $\rho_{xx} - T$ curves for the L_m/C_n SLs on LSAT are presented in Fig. 2d–f, demonstrating a similar change trend as the SLs on STO. Compared to the insulating phase of the L_2/C_1 and L_3/C_1 SLs, a metallic phase that maintains the lowest temperature of ~100 K is obtained in the L_2/C_4 and L_3/C_4 SLs (see Supplementary Fig. 5).

To better appreciate the thickness-dependent effect, Fig. 2g compares the conductivity at 300 K (σ_{300}) for all samples. Obviously, as the CTO inserting layer increases from 1 u.c. to 4 u.c., the conductance of the LNO layers is enhanced by a factor of ~45 for the 2 u.c.-thick LNO layers, ~12 for the 3 u.c.-thick LNO layers and ~2 for the 4 u.c.-thick LNO layers. It strongly suggests that the CTO layer has an capability to improve the conduction of the neighboring LNO layer. To reveal what causes the changes in transport properties, the Hall measurements were further performed for the SLs. The Hall curves at 300 K are given in Supplementary Fig. 6, indicating the hole-type conduction for the L_m/C_n SLs. Thus deduced carrier density and mobility at 300 K is summarized in Fig. 2h and Supplementary Table 1, as a function of t_{LNO} and t_{CTO}. We find that, at room temperature, the conduction enhancement with the increase of CTO layer thickness is primarily due to the rising of carrier density, while the carrier mobility is nearly unchanged. Further Hall analysis indicates that the CTO layer insertion would increase the carrier mobility of the LNO layer at low temperatures. For example, the carrier mobility of the L_4/C_4 at 5 K is enhanced by 5 times as compared to that of L_4/C_1 (see Supplementary Table 2). Thus, at low temperatures, the conduction enhancement is caused by the combined effects of a higher carrier density and the improved carrier mobility.

It should be further noticed that though the metallic state is achieved in ultrathin LNO layers at high temperatures, a resistance upturn is always preferred at low temperatures, accompanied by the hysteresis behavior while cooling and warming for some samples. This is a clear indication of first-order phase transition. Notably, such a thermal hysteresis loop in $\rho_{xx} - T$ curves have never been observed before in LNO films, though a highly insulating state has been reported for ultrathin LNO films. This phenomenon reminds us of other nickelates such as $NdNiO_3$ and $PrNiO_3$, which have orthorhombic symmetry with $a^-a^-c^+$ OOR pattern at room temperature. As temperature decreases, $NdNiO_3$ and $PrNiO_3$ undergo the first-order phase transition from the orthorhombic phase to the lower symmetry $P2_1/n$ monoclinic phase[37,38], accompanied by the MIT with obvious thermal hysteresis. Thus, the hysteresis behavior observed here implies that the LNO layers sandwiched between CTO layers may have a similar OOR pattern. To examine the onset temperature of the thermal hysteresis (T_{cr}), Fig. 2(i) plots the first derivative of resistivity with respect to temperature (dρ/dT) for several typical samples, where the onset temperature of the thermal hysteresis (T_{cr}) can be clearly identified. The deduced T_{cr} of the SLs are summarized in Supplementary Table 3. The T_{cr} is lowered by the increase of CTO layer thickness, suggesting the stabilization of the metallic phase in the SLs with thick CTO layers. As for the SLs on different substrates, the T_{cr} of SLs on LSAT is always lower than that of SLs on STO (see Supplementary Table 3). This is similar to the results of the orthorhombic-structured $NdNiO_3$ films deposited on LSAT or STO substrate[39], where the reduced tensile strain of LSAT substrate was believed to be the reason. In Supplementary Fig. 7, we further compare the $\rho_{xx} - T$ curves of the $[L_2/C_n]_2$ SLs on STO, LSAT, and $NdGaO_3$ (110) substrates. The changing trend of resistivity with the increase of CTO layer thickness is nearly the same for the SLs on all substrates, independent of substrate strain. Moreover, the $[L_2/C_4]_2$ SL on $NdGaO_3$ (110) shows the lowest resistivity, which may be due to the combined effects of the smallest tensile strain and the enhanced orthorhombic tilting.

Characterization of oxygen octahedron rotation

As mentioned in the introduction section, the degree or pattern of NiO_6 OOR is intimately linked to the electronic structure of nickelates, offering a promising strategy for tailoring the transport behavior of the nickelates. To determine the OOR in LNO/CTO SLs, we measured the Bragg peaks with half-integer indices, which appear when the pseudocubic unit cell is doubled due to octahedral rotations[8–11]. The presence or absence of a distinctive set of half-order peaks reveals the rotational pattern of oxygen octahedra, while the peak intensities provide information about the degrees of the octahedron rotations[40–43]. In Fig. 3a–c, we depict the half-order peaks of the L_3/C_n series of SLs. For comparison, the results of the LNO and CTO bare films are also given in Supplementary Fig. 8. Firstly, the L_3/C_1 SL exhibits Bragg peaks with half-integer index h, k, and l (n/2, where n is an odd integer, and $h = k \neq l$, $k = l \neq h$, and $h = l \neq k$). The typical peak indices are (1/2 3/2 1/2), (3/2 1/2 1/2), (1/2 1/2 3/2). This set of half-order peaks indicates the presence of an $a^-a^-c^-$ OOR pattern in the L_3/C_1 SL, consistent with the LNO thick films (see Supplementary Fig. 8). An interesting thing is that the half-order peak patterns unveil a striking behavior when the CTO layer thickness exceeds 1 u.c. In addition to the (1/2 3/2 1/2), (3/2 1/2 1/2), (1/2 1/2 3/2) peaks, a (1/2 3/2 1) peak is also observed in the L_3/C_2 and L_3/C_4 SLs. According to the Glazer rules[42,43], the appearance of (h k l) reflection with $h \neq k = n/2$ and an integer l signifies the in-phase c^+ rotation and rules out the out-of-phase c^- rotation, i.e., the OOR pattern turns to $a^-a^-c^+$ for the L_3/C_2 and L_3/C_4 SLs. As mentioned by previous works[44,45], the orthorhombic phase of ABO_3 oxides would demonstrate the antipolar-motion of A-cations, which could be used to determine the long axis of the orthorhombic structure. Detailed analysis on the antipolar-motion of A-cations in the L_4/C_4 SL is given in Supplementary Fig. 9. It confirms that both the CTO and the LNO sublayers have turned to the $a^-a^-c^+$ OOR pattern in the SL. This is interesting since it is distinct from the original ones ($a^-a^-c^-$ or $a^-b^+a^-$) of the LNO and CTO bare films. Moreover, the intensities of (1/2 3/2 1/2), (3/2 1/2 1/2), and (1/2 1/2 3/2) reflections decrease significantly from L_3/C_2 to L_3/C_4 as show in Supplementary Fig. 10a, though they have the same $a^-a^-c^+$ OOR pattern. According to Supplementary Fig. 10c, the (1/2 1/2 3/2) reflection could be generated by the a^- and b^- rotations, while the (1/2 3/2 1/2) (or (3/2 1/2 1/2)) reflections could be generated by the a^- and c^- (or b^- and c^-) rotations, respectively. As the c^- rotation mode has been ruled out by the appearance of the (1/2 3/2 1) reflection, the intensities of the (1/2 3/2 1/2), (3/2 1/2 1/2), and (1/2 1/2 3/2) reflections are mainly determined by the in-plane a^- and b^- rotations. Thus, their reduced intensities, from the L_3/C_2 SL to the L_3/C_4 SL, strongly suggest that the octahedral rotations along the in-plane **a**- and **b**-axes, referred to the OOR angle α and β, are significantly suppressed by the increase of CTO layer thickness.

To gain a deep insight into the OOR at the LNO/CTO heterointerface, integrated differential phase contrast (iDPC) STEM imaging was employed to quantify the layer-resolved octahedron tilting/rotation[34]. The L_4/C_4 SL was used as an example for this analysis (Fig. 3d). The in-plane tilting angle of Ni-O-Ni or Ti-O-Ti bond ($\theta_{Ni\text{-}O\text{-}Ni}$ or $\theta_{Ti\text{-}O\text{-}Ti}$) can be directly determined from the splitting of oxygen sites, as overlaid in the enlarged iDPC image. We can see that the oxygen site splitting is more significant in the CTO layers as compared to the LNO layers. To quantify the changes in the tilting angle, Fig. 3e presents the layer-by-layer $\theta_{Ni\text{-}O\text{-}Ni}$ and $\theta_{Ti\text{-}O\text{-}Ti}$ bond angles, obtained by averaging 20 unit cells per layer. As expected, the OOR is coupled at LNO/CTO

https://doi.org/10.1038/s41467-024-54311-0

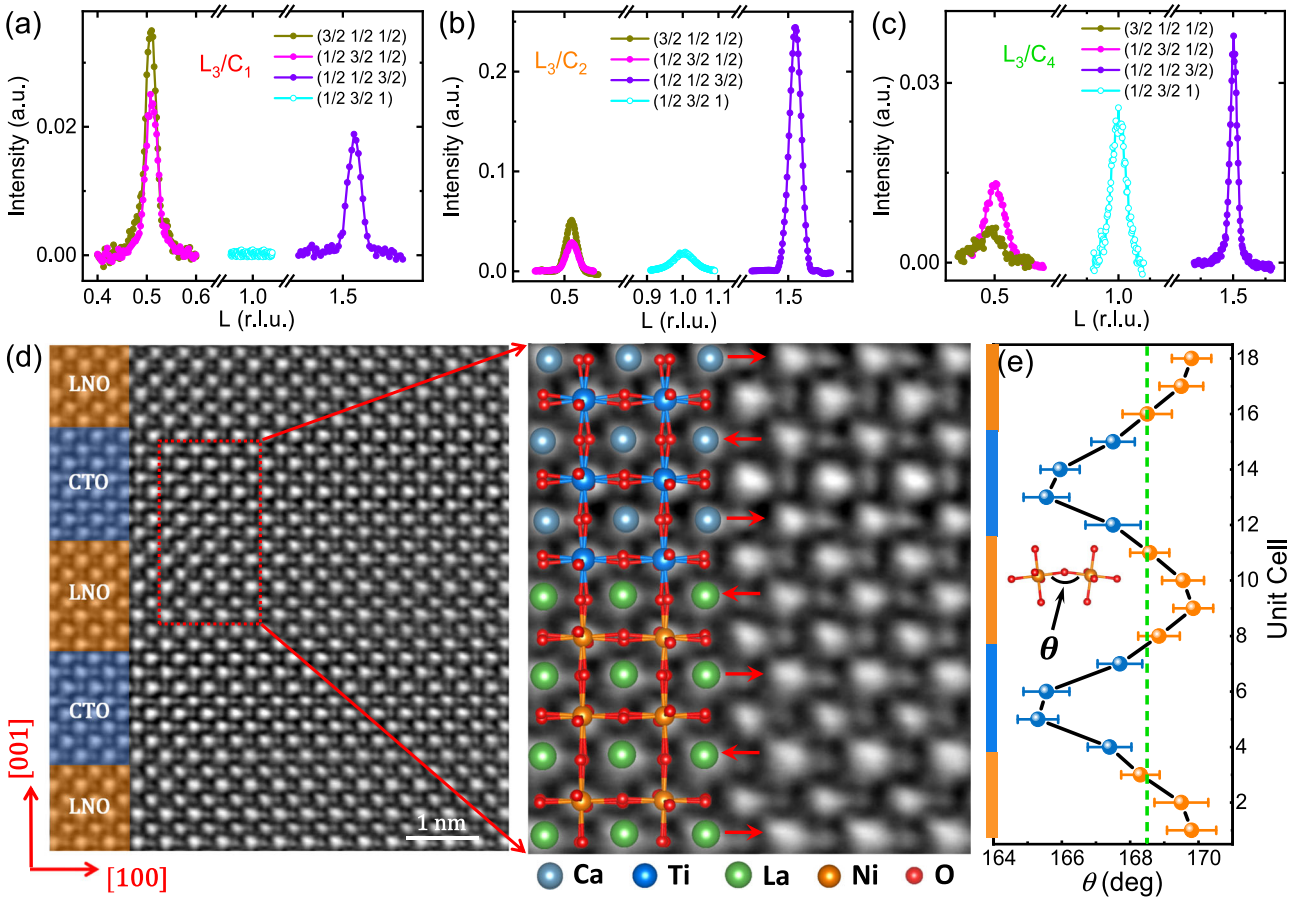

Fig. 3 | Characterization of Oxygen Octahedron Rotation. a Half-order peaks obtained from the L_3/C_1, **b** L_3/C_2 and **c** L_3/C_4 SLs on STO substrates. **d** iDPC-STEM image of a cross-section of L_4/C_4 SL. To clearly show octahedral tilting, the networks of NiO_6 and TiO_6 octahedra are superimposed on the enlarged image. The red arrows indicate the A-site antipolar displacements. **e** Layer-dependent tilting angle $\theta_{B\text{-}O\text{-}B}$, obtained by averaging 20 unit cells along [100] direction, where B represents Ni or Ti for different layers. The error bars denote the standard deviation of multiple measurements. The green dashed line indicates the tilting angle of the LNO bulk. The $\theta_{B\text{-}O\text{-}B}$ bond angle is sketched in the inset plots.

interface, resulting in the very close bond angle for the nearest LNO and CTO layer ($\theta_{Ni\text{-}O\text{-}Ni}$~168.5° and $\theta_{Ti\text{-}O\text{-}Ti}$~167.5°). A larger Ni-O-Ni bond angle (or lower Ti-O-Ti bond angle) is obtained for the second LNO (or CTO) layer from the interface. It should be pointed out that, the Ni-O-Ni angles of the LNO layers in the L_4/C_4 SL are comparable to or even greater than that obtained in bulk LNO or thick LNO films (168.5°)[8–10]. This is quite different from the ultrathin LNO bare films with insulating behavior, where the NiO_6 octahedra were highly distorted with a Ni-O-Ni bond angle of 153°~157°[29,46].

Previous work reported that the CTO engineered with proper OOR would become polar and even ferroelectric[33], which could also affect the conductivity of the nearby LNO layers[47,48]. Considering this possible mechanism, we conducted the optical SHG measurements on the L_4/C_4 SL, and no reliable signals were obtained (see Supplementary Fig. 11). It indicates that the centro-symmetricity in the SL system is not broken, making it impossible to generate ferroelectricity. This is reasonable since the CTO layer in the L_m/C_n SLs has the Pbnm symmetry that is non-polar according to the previous DFT calculation[33]. The above XAS results also rule out the interfacial charge transfer as the reason for the conductivity enhancement of LNO layers in the SLs. Thus, we consider that the OOR modulation of LNO by interface coupling is the most likely mechanism.

X-ray Spectroscopic Measurements

It is well acknowledged that the energy levels of the O-2p band and the Ni-3d band in nickelates are in close proximity, exhibiting a pronounced hybridization between them and thus forming the conduction band in LNO (Fig. 4a). The separation between the O-2p and Ni-3d orbitals is known as the charge transfer energy Δ, which is primarily controlled by the Ni-O-Ni bond length and bond angle[12–14]. Thus, it is reasonable that a large Ni-O-Ni bond angle of the LNO layers in the LNO/CTO heterostructure will favor an enhanced orbital overlap, supporting the metallic behavior. To gain an insight into the electronic structure and the orbital hybridization, soft XAS measurements were performed for the LNO/CTO SLs. As reported by Van Veenendaal et al. [49], changes in the multiplet splitting of the Ni L_3 absorption edge could be used to estimate the degree of covalence between Ni 3d and O 2p bands. This splitting corresponds to the energy separation Δ between the t_{2g} and e_g levels of Ni, which is determined by the interplay between orbital hybridization and Coulomb repulsion. Previous studies on ultrathin LNO films have shown that the large splitting of the Ni L_3 peak is responsible for the occurrence of electronic dead layer[35,50]. In the present work, we analyzed the XAS spectra around the Ni L_3 edge for the L_m/C_n SLs, along with two reference data obtained from a thick (~25 u.c.) and a thin (~2 u.c.) LNO bare films. Figure 4b and Supplementary Fig. 12 present the normalized spectra of the Ni L_3 edge for the L_m/C_n SLs on STO substrates. Since the La M_4 line partially overlaps the Ni L_3 contribution, corrections have been made to the Ni L_3 edge signals (see Supplementary Fig. 13). As expected, the Ni L_3 edge splits into two primary peaks, and the splitting enhances as n decreases. To quantify the observed multiplet splitting energy, we fitted the Ni L_3 spectra with the sum of two peaks for all samples. The resulting energy splitting is shown in Fig. 4c, as a function of CTO layer thickness. For the L_2/C_1 SL, the Ni L_3 splitting energy is ~1.48 eV, close to that of the 2 u.c.-thick LNO bare film (1.53 eV).

https://doi.org/10.1038/s41467-024-54311-0

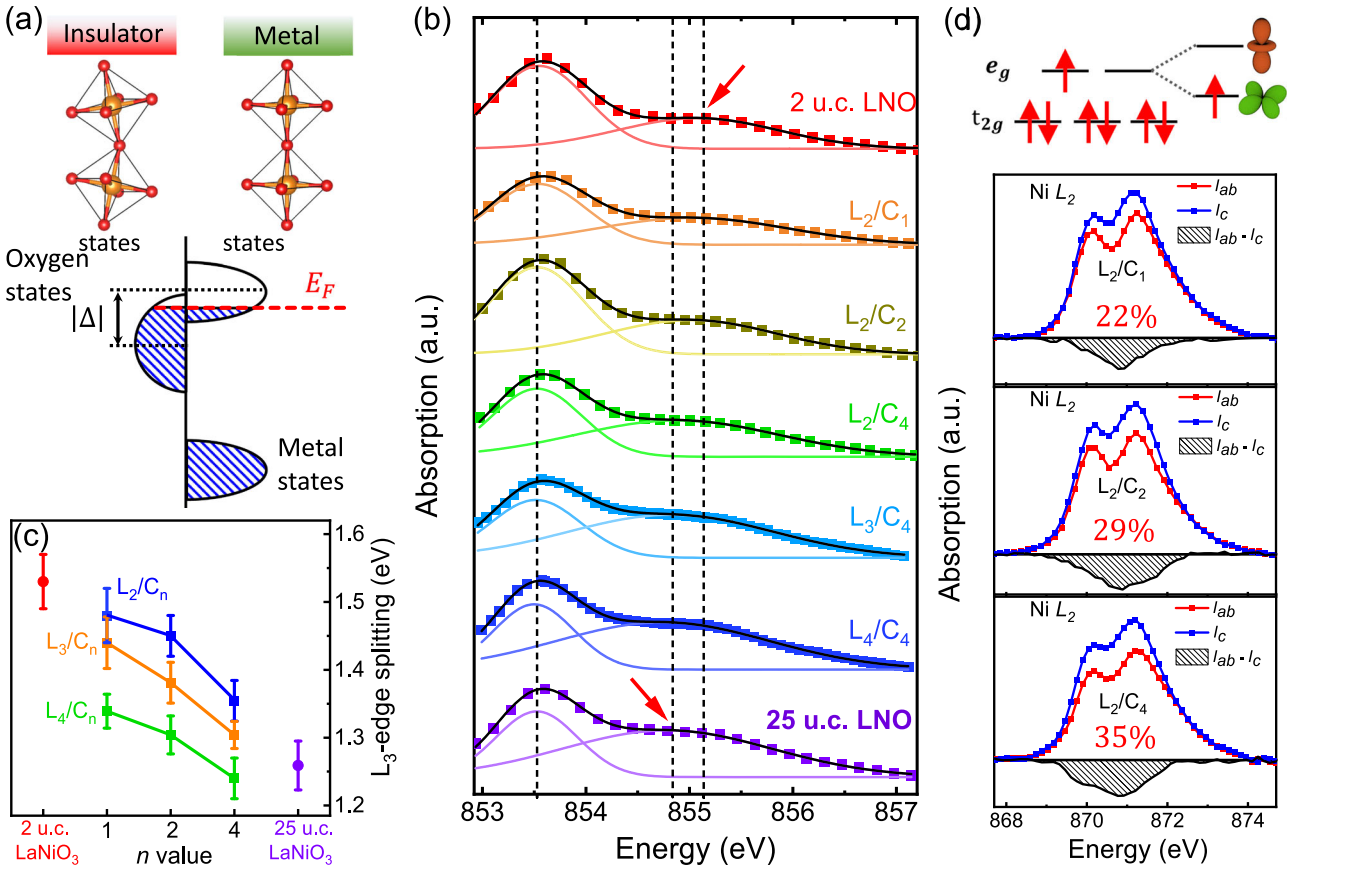

Fig. 4 | X-ray spectroscopic measurements. a Band scheme proposed to explain the transport behavior of $LaNiO_3$, where the overlapped Ni^{3+} and O^{2-} bands give the metallic behavior. The shadow region shows the occupied band states. **b** X-ray absorption spectroscopy (XAS) of the Ni L_3 edge and the fitting of Ni L_3 spectra with the sum of two peaks for selected SLs. The arrows indicate the position of the second peak. Vertical dashed lines are guides for eyes to view the shift of peak position. **c** Splitting energy as a function of *n*, extracted from the curve fitting of the Ni L_3 edge of SLs. The error bars represent the standard error obtained from the fitting process. **d** X-ray linear dichroism (XLD) data, obtained around the Ni L_2-edge of the L_2/C_1, L_2/C_2, and L_2/C_4 SLs. Blue and red curves represent the intensities of I_c and I_{ab}, respectively. The black curve is the XLD spectrum deduced from ($I_{ab} - I_c$).

Subsequently, the splitting energy decreases to 1.45 eV and to 1.35 eV when the CTO inserting layer increases from 1 u.c. to 2 u.c. and to 4 u.c. This trend is also observed in the series of L_3/C_n and L_4/C_n SLs. Especially, the splitting energy of the L_4/C_4 SL (1.24 eV) is already comparable to that of the 25 u.c.-thick LNO bare film (1.26 eV). Obviously, it is the enhancement of Ni 3d-O 2p hybridization with increased CTO layer thickness (reflected by the decrease in charge-transfer energy Δ) that stabilizes the metallic phase in ultrathin LNO layers.

Now we turn our attention to the reconstruction of the Ni e_g orbital in the LNO/CTO heterostructure. Figure 4d displays the x-ray linear dichroism (XLD) studies conducted on the Ni L_2-edge of the L_2/C_1, L_2/C_2, and L_2/C_4 SLs. The orbital configuration of Ni is probed by the difference in intensity between I_{ab} (x-ray polarization parallel to the in-plane [100]) and I_c (x-ray polarization parallel to the out-of-plane [001]). Here, the I_c was corrected by considering the incident angle of 30° between the x-ray and sample plane (see details in the experimental section). A negative XLD signal ($I_{ab} - I_c$) is observed for all L_2/C_n SLs, indicating the preferred occupation of the $d_{x^2-y^2}$ orbital. By integrating the intensities of I_{ab} and I_c in the 867–875 eV range (after subtracting background), the ratio of holes in the e_g orbitals can be quantified by the following equation[20,23–25]:

$$r = \frac{h_{3z^2-r^2}}{h_{x^2-y^2}} = \frac{3I_c}{4I_{ab} - I_c} \quad (1)$$

where *r* is the hole ratio, $h_{3z^2-r^2}$ and $h_{x^2-y^2}$ are the number of holes in the orbital $d_{3z^2-r^2}$ and $d_{x^2-y^2}$, respectively. For bulk LNO, $r = 1$ was reported, indicating the fully degenerated e_g orbitals[18–20]. The *r* values for the L_2/C_1, L_2/C_2, and L_2/C_4 SLs are 1.22, 1.29, and 1.35, respectively. This suggests that the relative change of occupancy *r*-1 is as high as 35% for the LNO/CTO SLs, significantly larger than the values of ~19% and ~3% induced by lattice strains and spatial confinement, respectively[23–26]. The orbital polarization can be also estimated by another quantity *P*, defined as:

$$P = \frac{n_{x^2-y^2} - n_{3z^2-r^2}}{n_{x^2-y^2} + n_{3z^2-r^2}} = \left(\frac{4}{n_{e_g}} - 1\right)\frac{r-1}{r+1} \quad (2)$$

where $n_{3z^2-r^2}$ and $n_{x^2-y^2}$ are the number of electrons in the orbital $d_{3z^2-r^2}$ and $d_{x^2-y^2}$, respectively. Unlike *r*, *P* is sensitive to the choice of local atomic basis, i.e. the total occupancy of the e_g manifold (n_{eg}), which shows fairly large variations from 1.5 to 2.1 reported in different literature[51,52]. Using an average value of $n_{eg} = 1.8$ for estimation, we obtained the positive values of *P* up to 18% for the LNO/CTO SLs, much higher than that observed in previous works (5–9%)[18,25,26]. To the best of our knowledge, this is the largest in-plane orbital polarization in ultrathin LNO layers, illustrating the strong impact of the OOR on orbital reconstruction.

Theoretical Analysis

To understand the relationship between electronic structure and macroscopic properties, the band structure and density of states (DOS) of the L_3/C_1, L_3/C_2, and L_3/C_4 SLs are further investigated by the

https://doi.org/10.1038/s41467-024-54311-0

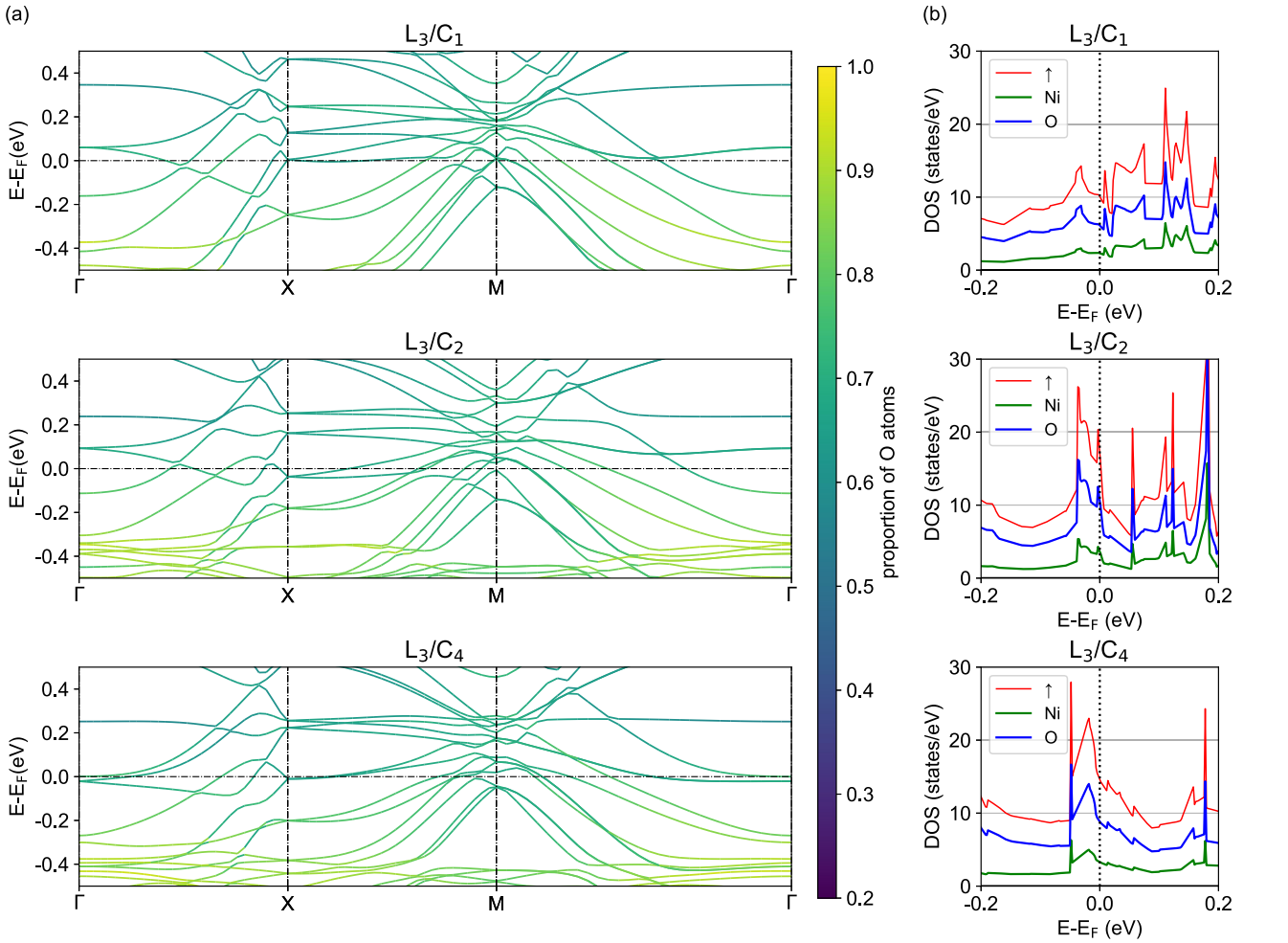

Fig. 5 | The band structure and density of states (DOS) of LNO/CTO SLs. a O atom projected band structure and **b** spin up the density of states for the L_3/C_1, L_3/C_2, and L_3/C_4 SLs. The color bar describes the proportion of O atoms. The DOS at the Fermi level is 10.01, 13.23, and 15.08 states/eV corresponding to the L_3/C_1, L_3/C_2, and L_3/C_4 SLs (after subtracting the sharp DOS peak at the Fermi level).

density functional theory (DFT) calculations. The basic parameters of the initial structure for structural optimization are obtained from the experimental results. The results of structure optimization show that the stable structure assumes $a^-a^-c^-$ OOR pattern for L_3/C_1 and $a^-a^-c^+$ OOR pattern for both L_3/C_2 and L_3/C_4, which is consistent with the experimental observations (see Supplementary Fig. 14). The calculated band structures and DOS are shown in Fig. 5. The band structure and DOS are spin-polarized and there is one spin channel (spin up) in the energy range −0.4 eV to 0.4 eV. The atom-projected band structures indicate that the low-energy bands (near the Fermi level) originate mainly from O atoms. About 70% of the DOS are associated with O atoms and 30% are associated with Ni atoms. Therefore, the conductivity originates from the electronic states contributed by Ni and O atoms. The weights of O and Ni atoms, matching the calculated projected band structure, indicate the orbital hybridization between O atoms and Ni atoms. The trend of conductivity for the L_3/C_1, L_3/C_2, and L_3/C_4 SLs can be explained in terms of the band structures and the corresponding DOS values at the Fermi level. The band structures of L_3/C_1 and L_3/C_2 are similar on a large scale, but flat bands are observed near the Fermi level in L_3/C_1, which contributes little to the conductivity. In addition, L_3/C_2 has a larger DOS at the Fermi level than L_3/C_1 does. For the comparison of L_3/C_1 and L_3/C_2, we need to subtract the sharp DOS peak at the Fermi level because it results from flat bands and contributes little to conductivity. These features explain the phenomenon why L_3/C_2 has a lower resistance than L_3/C_1. As for the comparison of L_3/C_2 and L_3/C_4, the main point is that L_3/C_4 has more bands and larger DOS at the Fermi level than L_3/C_2 does after subtracting the sharp peak, which indicates that L_3/C_4 has more effective carriers than L_3/C_2 does. In addition, the slope of the band curves of L_3/C_4 is larger than that of L_3/C_2, which may reduce the effective mass of carriers, leading to higher mobility. Therefore, L_3/C_4 has higher conductivity than L_3/C_2.

Discussion

In summary, we demonstrate an approach to stabilize a nonequilibrium OOR pattern of $a^-a^-c^+$ in the LNO sublayers of the LNO/CTO SLs. Unlike the $a^-a^-c^-$ pattern in LNO bare films, the metastable $a^-a^-c^+$ OOR pattern is found to favor the metallic state in the LNO ultrathin layers with a thickness down to 2 u.c. More importantly, a strong $d_{x^2-y^2}$ orbital polarization is simultaneously achieved in the 2 u.c.-thick $LaNiO_3$ layers, with the highest change of occupancy of 35% or orbital polarization of 18%. These values are significantly larger than those achieved from other approaches, such as strain effect, spatial confinement or interfacial charge transfer. XAS results indicate that the modulated OOR pattern of LNO in the LNO/CTO SLs has significantly enhanced the Ni-3d/O-2p hybridization, stabilizing the metallic state in LNO ultrathin films. The simultaneous realization of the metallic conduction and larger $d_{x^2-y^2}$ orbital polarization in LNO ultrathin layers fulfills the basic properties of carriers in high *Tc* superconducting cuprates (no orbital degeneracy, spin one half, quasi-2D confinement, and antiferromagnetic correlations), showing a feasible way for searching superconductivity in LNO-based heterostructures.

Methods

Sample fabrication and characterizations

High-quality $[LNO_m/CTO_n]_8$ SLs were epitaxially grown on (001)-oriented STO and LSAT substrates by the technique of pulsed laser deposition (KrF, λ = 248 nm). During film growth, the substrate temperature was kept at 620 °C and the oxygen pressure was set to 20 Pa. The adopted fluence of laser pulse was 1.2 J/cm^2 and the repetition rate was 2 Hz. The deposition rate for the LNO and CTO layers has been carefully calibrated by the technique of small angle x-ray reflectivity (XRR, see Supplementary Fig. 1). The surface morphology of as-prepared films was measured by atomic force microscopy (AFM, SPI 3800 N, Seiko). The crystal structure was determined by a high-resolution X-ray diffractometer (D8 Discover, Bruker) with the Cu-Kα radiation. The transport measurements were performed in Quantum Designed physical property measurement system (PPMS) with standard Hall bar geometry.

Integrated differential phase contrast (iDPC) STEM imaging and analysis

Atomically resolved HAADF-STEM and iDPC-STEM experiments were carried out on a FEI Titan Cubed Themis 60-300 (operating at 300 kV), which was capable of recording high-resolution STEM images with a spatial resolution of ≈0.06 nm. The microscopy equipment included a high-brightness electron gun (X-FEG with a monochromator), a C_S probe corrector, a C_S image corrector, and a postcolumn imaging energy filter (Gatan Quantum 965 Spectrometer). The collection angle of the HAADF detector was 64–200 mrad, and the iDPC image was acquired by a segmented DF4 detector with 4 quadrants. For this experiment, a convergence angle of 21 mrad was used, and the sample was kept at room temperature.

Half-order diffraction peaks measurements

The oxygen positions are determined by the measurement and analysis of half-order diffraction peaks arising from the doubling of the unit cell due to octahedral rotations. The presence and absence of specific half-order peaks reveal the rotational pattern, while the magnitudes of the octahedral rotations are determined from the peak intensities. The half-order Bragg peak of the samples was systematically investigated at room temperature on Huber5020 six-circle diffractometer at the beamline BL02U2 in the Shanghai Synchrotron Radiation Facility.

X-ray spectroscopic measurements

The X-ray absorption spectroscopy (XAS) measurements are performed at the beamline BL08U1A in the Shanghai Synchrotron Radiation Facility at room temperature in a total electron yield mode. The spectra of Ni L edge are measured by changing the incident angle of the linearly polarized x-ray beam. The sample's scattering plane was rotated by 30° and 90° with respect to the incoming photons. When the X-ray beam is perpendicular to the surface plane, the XAS signal directly reflects the $3d_{x^2-y^2}$ orbital occupancy. While the angle between the x-ray beam and surface plane is 30°, the XAS signal contains orbital information from both $3d_{x^2-y^2}$ and $3d_{3z^2-r^2}$ orbitals. Therefore, for simplifying the results, the unoccupied in-plane orbital states are proportional to $I_{ab} = I_{90°}$, while the unoccupied out-of-plane orbital states can be calculated by $I_c = (I_{90°} - I_{30°}\cdot\sin^2 30°)/\cos^2 30°$. XLD is calculated by $I_{ab} - I_c$.

First-principles calculations

All first-principles calculations are performed with the projector-augmented wave method within the density functional theory[53], as implemented in the Vienna ab initio simulation package software[54]. The generalized gradient approximation by Perdew, Burke, and Ernzerhof is used as the exchange-correlation functional[55]. The self-consistent calculations are carried out with a Γ-centered (6 × 6 × 1) Monkhorst–Packgrid[56]. The kinetic energy cutoff of the plane wave is set to 450 eV. The convergence criteria of the total energy and force are set to 10^{-6} eV and 0.05 eV Å^{-1}. The Hubbard-U term (U = 6 eV) is considered for Ni in the DFT + U scheme to improve energy band description[57].

Data availability

The data that supports the findings of this study are available at https://zenodo.org/records/13957770. All other data are available from the corresponding authors upon request.

References

1. Catalan, G. Progress in perovskite nickelate research. *Phase Transit.* **81**, 729–749 (2008).
2. María Luisa, M. Structural, magnetic and electronic properties of perovskites (R = rare earth). *J. Condens. Matter Phys.* **9**, 1679 (1997).
3. Torrance, J. B., Lacorre, P., Nazzal, A. I., Ansaldo, E. J. & Niedermayer, C. Systematic study of insulator-metal transitions in perovskites $RNiO_3$ (R=Pr, Nd, Sm, Eu) due to closing of charge transfer gap. *Phy. Rev. B* **45**, 8209–8212 (1992).
4. García-Muñoz, J., Rodríguez-Carvajal, J., Lacorre, P. & Torrance, J. Neutron-diffraction study of $RNiO_3$ (R = La, Pr, Nd, Sm): electronically induced structural changes across the metal-insulator transition. *Phys. Rev. B* **46**, 4414–4425 (1992).
5. Mercy, A., Bieder, J., Iniguez, J. & Ghosez, P. Structurally triggered metal-insulator transition in rare-earth nickelates. *Nat. Commun.* **8**, 1677 (2017).
6. Chen, B. et al. Spatially controlled octahedral rotations and metal–insulator transitions in nickelate superlattices. *Nano Lett.* **21**, 1295–1302 (2021).
7. Liao, Z. et al. Metal–insulator-transition engineering by modulation tilt control in perovskite nickelates for room temperature optical switching. *Proc. Natl Acad. Sci. USA* **115**, 9515–9520 (2018).
8. May, S. J. et al. Quantifying octahedral rotations in strained perovskite oxide films. *Phys. Rev. B* **82**, 014110 (2010).
9. Fowlie, J. et al. Thickness-dependent perovskite octahedral distortions at heterointerfaces. *Nano Lett.* **19**, 4188–4194 (2019).
10. May, S. J. et al. Control of octahedral rotations in $(LaNiO_3)_n/(SrMnO_3)_m$ superlattices. *Phys. Rev. B* **83**, 153411 (2011).
11. Tung, I. C. et al. Connecting bulk symmetry and orbital polarization in strained $RNiO_3$ ultrathin films. *Phys. Rev. B* **88**, 205112 (2013).
12. Medarde, M. et al. $RNiO_3$ perovskites (R=Pr, Nd): Nickel valence and the metal-insulator transition investigated by x-ray-absorption spectroscopy. *Phys. Rev. B Condens. Matter* **46**, 14975–14984 (1992).
13. Grisolia, M. N. et al. Hybridization-controlled charge transfer and induced magnetism at correlated oxide interfaces. *Nat. Phys.* **12**, 484 (2016).
14. Sanchez, R. D. et al. Metal-insulator transition in oxygen-deficient $LaNiO_{3-x}$ perovskites. *Phys. Rev. B* **54**, 16574 (1996).
15. Keimer, B., Kivelson, S. A., Norman, M. R., Uchida, S. & Zaanen, J. From quantum matter to high-temperature superconductivity in copper oxides. *Nature* **518**, 179–186 (2015).
16. Zhang, F. C. & Rice, T. M. Effective Hamiltonian for the superconducting Cu oxides. *Phys. Rev. B* **37**, 3759–3761 (1988).
17. Lee, P. A., Nagaosa, N. & Wen, X.-G. Doping a Mott insulator: physics of high-temperature superconductivity. *Rev. Mod. Phys.* **78**, 17 (2006).
18. Cao, Y. et al. Engineered Mott ground state in a $LaTiO_{(3+\delta)}/LaNiO_3$ heterostructure. *Nat. Commun.* **7**, 10418 (2016).
19. Golalikhani, M. et al. Nature of the metal-insulator transition in few-unit-cell thick $LaNiO_3$ films. *Nat. Commun.* **9**, 1–8 (2018).
20. Liao, Z. et al. Large orbital polarization in conductivity and local structure of $LaNiO_3$ thin films nickelate-cuprate heterostructures by dimensional control of oxygen coordination. *Nat. Commun.* **10**, 589 (2010).

21. Chaloupka, J. & Khaliullin, G. Orbital order and possible superconductivity in $LaNiO_3/LaMO_3$ superlattices. *Phys. Rev. Lett.* **100**, 016404 (2008).
22. Hansmann, P. et al. Turning a nickelate fermi surface into a cupratelike one through heterostructuring. *Phys. Rev. Lett.* **103**, 016401 (2009).
23. Wu, M. et al. Strain and composition dependence of orbital polarization in nickel oxide superlattices. *Phys. Rev. B* **88**, 125124 (2013).
24. Chen, B. et al. Strain-engineered metal-to-insulator transition and orbital polarization in nickelate superlattices integrated on silicon. *Adv. Mater.* **32**, 2004995 (2020).
25. Benckiser, E. et al. Orbital reflectometry of oxide heterostructures. *Nat. Mater.* **10**, 189–193 (2011).
26. Freeland, J. W. et al. Orbital control in strained ultra-thin $LaNiO_3/LaAlO_3$ superlattices. *Europhys. Lett.* **96**, 57004 (2011).
27. Scherwitzl, R. et al. Metal-insulator transition in ultrathin $LaNiO_3$ films. *Phys. Rev. Lett.* **106**, 246403 (2011).
28. Hao, Y. et al. Record high room temperature resistance switching in ferroelectric-gated Mott transistors unlocked by interfacial charge engineering. *Nat. Commun.* **14**, 8247 (2023).
29. Fowlie, J. et al. Conductivity and local structure of $LaNiO_3$ thin films. *Adv. Mater.* **29**, 1605197 (2017).
30. Son, J. et al. Low-dimensional Mott material: transport in ultrathin epitaxial $LaNiO_3$ films. *Appl. Phys. Lett.* **96**, 062114 (2010).
31. King, P. D. C. et al. Atomic-scale control of competing electronic phases in ultrathin $LaNiO_3$. *Nat. Nanotechnol.* **9**, 443–447 (2014).
32. Sakai, E., Tamamitsu, M., Yoshimatsu, K., Okamoto, S. & Horiba, K. Gradual localization of Ni 3d states in $LaNiO_3$ ultrathin films induced by dimensional crossover. *Phys. Rev. B* **87**, 075132 (2013).
33. Kim, J. R. et al. Stabilizing hidden room-temperature ferroelectricity via a metastable atomic distortion pattern. *Nat. Commun.* **11**, 4944 (2020).
34. Hoglund, E. R. et al. Emergent interface vibrational structure of oxide superlattices. *Nature* **601**, 556–561 (2022).
35. Lu, X. et al. Dimensionality-controlled evolution of charge-transfer energy in digital nickelates superlattices. *Adv. Sci.* **9**, 2105864 (2022).
36. Disa, A. S. et al. Orbital engineering in symmetry-breaking polar heterostructures. *Phys. Rev. Lett.* **114**, 026801 (2015).
37. Johnston, S., Mukherjee, A., Elfimov, I., Berciu, M. & Sawatzky, G. A. Charge disproportionation without charge transfer in the rare Earth-element nickelates as a possible mechanism for the metal-insulator transition. *Phys. Rev. Lett.* **112**, 106404 (2014).
38. García-Muñoz, J. L., Aranda, M. A. G., Alonso, J. A. & Martínez-Lope, M. J. Structure and charge order in the antiferromagnetic band-insulating phase of $NdNiO_3$. *Phys. Rev. B* **79**, 134432 (2009).
39. Heo, S., Oh, C., Son, J. & Jang, H. M. Influence of tensile-strain induced oxygen deficiency on metal-insulator transitions in $NdNiO_{3-\delta}$ epitaxial thin films. *Sci. Rep.* **7**, 4681 (2017).
40. He, F., Wells, B. O. & Shapiro, S. M. Strain phase diagram and domain orientation in $SrTiO_3$ thin films. *Phys. Rev. Lett.* **94**, 176101 (2005).
41. Johnson-Wilke, R. L. et al. Quantification of octahedral rotations in strained $LaAlO_3$ films via synchrotron x-ray diffraction. *Phys. Rev. B* **88**, 174101 (2013).
42. Glazer, A. M. The classification of tilted octahedra in perovskites. *Acta Crystallogr. Sect. B* **28**, 3384–3392 (1972).
43. Glazer, A. Simple ways of determining perovskite structures. *Acta Cryst. A* **31**, 756–762 (1975).
44. Mundet, B. et al. Mapping orthorhombic domains with geometrical phase analysis in rare-earth nickelate heterostructures. *APL Mater.* **12**, 031124 (2024).
45. Varbaro, L. et al. Structural study of nickelate based heterostructures. *APL Mater.* **12**, 031104 (2024).
46. Kumah, D. P. et al. Tuning the structure of nickelates to achieve two-dimensional electron conduction. *Adv. Mater.* **26**, 1935–1940 (2014).
47. Hong, X., Posadas, A. & Ahn, C. H. Examining the screening limit of field effect devices via the metal-insulator transition. *Appl. Phys. Lett.* **86**, 142501 (2005).
48. Malashevich, A. et al. Controlling mobility in perovskite oxides by ferroelectric modulation of atomic-scale interface structure. *Nano Lett.* **18**, 573 (2018).
49. Piamonteze, C. et al. Spin-orbit-induced mixed-spin ground state in $RNiO_3$ perovskites probed by x-ray absorption spectroscopy: insight into the metal-to-insulator transition. *Phys. Rev. B* **71**, 020406 (2005).
50. Liu, J. et al. Quantum confinement of Mott electrons in ultrathin $LaNiO_3/LaAlO_3$ superlattices. *Phys. Rev. B* **83**, 161102 (2011).
51. Han, M. J., Marianetti, C. A. & Millis, A. J. Chemical control of orbital polarization in artificially structured transition-metal oxides: La_2NiXO_6 (X = B, Al, Ga, In) from first principles. *Phys. Rev. B* **82**, 134408 (2010).
52. Han, M. J., Wang, X., Marianetti, C. A. & Millis, A. J. Dynamical mean-field theory of nickelate superlattices. *Phys. Rev. Lett.* **107**, 206804 (2011).
53. Blöchl, P. E. Projector augmented-wave method. *Phys. Rev. B* **50**, 17953–17979 (1994).
54. Kresse, G. & Hafner, J. Ab initio molecular dynamics for liquid metals. *Phys. Rev. B Condens Matter* **47**, 558–561 (1993).
55. Perdew, J. P., Burke, K. & Ernzerhof, M. Generalized gradient approximation made simple. *Phys. Rev. Lett.* **77**, 3865–3868 (1996).
56. Monkhorst, H. J. & Pack, J. D. Special points for Brillouin-zone integrations. *Phys. Rev. B* **13**, 5188–5192 (1976).
57. Dudarev, S. L., Botton, G. A., Savrasov, S. Y., Humphreys, C. J. & Sutton, A. P. Electron-energy-loss spectra and the structural stability of nickel oxide: an LSDA+ U study. *Phys. Rev. B* **57**, 1505 (1998).

Acknowledgements

This work has been supported by the National Key R&D Program of China (Grants nos. 2023YFA1607400, 2022YFA1403302, 2023YFA1406400, and 2019YFA0704904), the Science Center of the National Science Foundation of China (Grant no. 52088101), the National Natural Science Foundation of China (Grants nos. T2394472, 11934016, 12274443, 12304149), and the Key Program of the Chinese Academy of Sciences. J.R.S. is thankful for the support of the Project for Innovative Research Team of the National Natural Science Foundation of China (Project no. 11921004). B.G L. is thankful for the Strategic Priority Research Program of the Chinese Academy of Sciences (Grant no. XDB33020100) and the Nature Science Foundation of China (Grant no.11974393). J. Z is thankful for the Guangdong Basic and Applied Basic Research Foundation (Grant nos. 2022A1515110648, 2023A1515010953). We acknowledge Beamline BL08U1A and BL02U2 in the Shanghai Synchrotron Radiation Facility (SSRF). This work was supported by the Synergetic Extreme Condition User Facility (SECUF).

Author contributions

W.X.S. carried out the sample fabrication and performed the transport, half-order diffraction peaks, and X-ray spectroscopic measurements. J.Z. (Jing Zhang) performed integrated differential phase contrast (iDPC) STEM imaging and analysis. B.W.Y. performed the theoretical calculation. Y.S.C. designed experiments, analyzed data and wrote the manuscript. J.Z. (Jie Zheng), M.Q.W. and Z.L. participated in sample fabrication and characterization. J.Y.Z. performed the SHG measurements. B.G.L., Y.Z.C., F.X.H. and B.G.S. discussed on physical mechanisms and DFT calculations. J.R.S. designed experiments and revised the manuscript. All authors discussed the progress of the research and reviewed the manuscript.

Competing interests

The authors declare no competing interests.

Additional information

Supplementary information The online version contains supplementary material available at https://doi.org/10.1038/s41467-024-54311-0.

Correspondence and requests for materials should be addressed to Banggui Liu, Yuansha Chen or Jirong Sun.

Peer review information *Nature Communications* thanks Hanjong Paik and the other, anonymous, reviewer(s) for their contribution to the peer review of this work. A peer review file is available.